

Do We Need Tensor Cores for Stencil Computations?

Qiqi Gu*
qiqi.gu@sjtu.edu.cn
Shanghai Jiao Tong University
Shanghai, China

Chenpeng Wu*
cpwu_sjtu@sjtu.edu.cn
Shanghai Jiao Tong University
Shanghai, China

Heng Shi†
heng.shi@sjtu.edu.cn
Shanghai Enflame Technology
Co.,Ltd.; Shanghai Jiao Tong
University
Shanghai, China

Jianguo Yao†
jianguo.yao@sjtu.edu.cn
Shanghai Jiao Tong University
Shanghai, China

Haibing Guan
hbguan@sjtu.edu.cn
Shanghai Jiao Tong University
Shanghai, China

Abstract

Stencil computation constitutes a cornerstone of scientific computing, serving as a critical kernel in domains ranging from fluid dynamics to weather simulation. While stencil computations are conventionally regarded as memory-bound and thus unsuitable for compute-centric Tensor Cores, recent empirical studies have demonstrated significant speedups after applying Tensor Cores, forming an apparent contradiction.

This paper resolves this contradiction by conducting a systematic performance analysis of stencil computations on Tensor Cores. We begin by revisiting the adaptation of stencils onto Tensor Cores, quantifying the computational redundancy introduced by the transformations required to satisfy hardware constraints. These metrics are subsequently integrated into an enhanced performance model that explicitly accounts for the arithmetic intensity shifts driven by temporal fusion. Guided by this formulation, we derive analytical criteria to determine the suitability of Tensor Cores for varying stencil workloads. By classifying operational regions, we identify the specific *sweet spot* for effective acceleration and further demonstrate how Sparse Tensor Cores expand this profitable design space. Extensive evaluations on NVIDIA GPUs across SOTA implementations, including DRStencil, EBISU, ConvStencil, and SPIDER, validate our performance model and analytical criteria. These results demonstrate the effectiveness of our approach in guiding stencil performance optimization.

Keywords

Stencil Computation, Performance Modeling, Tensor Core

1 Introduction

Stencil computation constitutes a foundational numerical method in which each grid point is updated via a weighted sum of its neighbors according to a fixed, pre-defined pattern. It serves as a cornerstone across diverse scientific domains, including fluid dynamics [22, 30], earth system modeling [23], weather simulation [6, 8], and wave

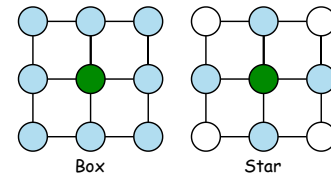


Figure 1: Stencil Computation Pattern.

propagation [5, 33], and is identified as one of the seven most critical numerical methods in science and engineering [7, 12]. A stencil computation can be characterized by three key parameters: shape, radius r (also referred to as *order*), and dimensionality d . As shown in Figure 1, common shapes include the box stencil, which incorporates all grid points within a hyper-rectangular neighborhood centered on the target point, and the star stencil, which includes only points aligned with the coordinate axes. The radius r defines the neighborhood extent, that is, the maximum distance from the center point, while the dimensionality d specifies whether the domain is 1D, 2D, 3D, or higher. For instance, the 2D Jacobi iterative method represents a typical example of a Star-2D1R stencil.

Conventionally, stencil computations are regarded as memory-bound workloads. This naturally stems from their workload pattern: a large number of memory accesses are required to fetch neighboring data points for each grid point update, while only a few computing operations are performed. For large-scale problems whose working sets exceed the capacity of the fast on-chip storage (e.g., registers or caches), frequent off-chip memory accesses become inevitable, placing significant pressure on memory bandwidth. Consequently, even though grid updates allow for massive parallelism, the system becomes memory-bound, leaving execution units idle. Consequently, attainable performance is typically limited by the bandwidth of the memory subsystem, rather than the theoretical compute throughput of the hardware.

To release the memory pressure and better utilize the limited memory bandwidth, researchers have extensively analyzed the access pattern and proposed numerous optimizations that exploit spatial and temporal locality. Spatial tiling, being a representative optimization technique, partitions the computational domain into smaller blocks, enabling data to reside in faster memory where it can be reused across multiple computations. Specialized tiling schemes,

*Equal Contribution

†Corresponding author

TBD, TBD

2026. ACM ISBN 000-0-0000-0000-0/00/00
<https://doi.org/XXXXXXXX.XXXXXXX>

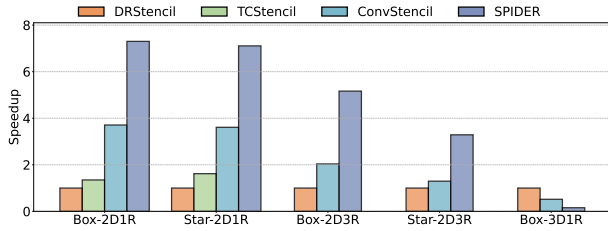


Figure 2: Performance Comparison between CUDA Core and Tensor Core Implementations.

including rectangular tiling [32, 37], cache-oblivious tiling [14, 39], and tessellating tiling [46], have been proposed to optimize stencil computations with a specific pattern. Another typical strategy is temporal fusion, it merges multiple time steps in a single computing kernel, exploiting inter-step locality to amortize memory access overhead. DRStencil [45] and EBISU [48] are two recent representatives that employ this optimization. Moreover, there exist some dedicated optimizations to better align with modern hardware features. For example, data layout transformations [19, 20, 24] reorganize memory representations to match hardware access patterns, reducing potential memory transaction amplification and resource contention, thus maximizing bandwidth utilization.

Given this inherent memory-bound nature of stencil computation, a long-standing consensus in the community is that emerging compute-centric Arithmetic Logic Units (ALUs), such as Tensor Cores and Matrix Cores, are not suitable for stencil workloads [47]. The rationale is straightforward: these units significantly increase compute throughput but offer no additional memory bandwidth compared to general-purpose ALUs (e.g., CUDA Cores), the performance of stencil kernels remains bounded by data movement. Therefore, simply adapting computations onto Tensor Cores theoretically yields negligible performance benefit over CUDA Cores.

Interestingly, recent empirical evidence contradicts this conventional assumption. Several cutting-edge studies successfully adapt stencil computations onto Tensor Cores, achieving substantial speedups. For example, TCStencil [29] first demonstrates the feasibility of adapting star- and box-shaped stencils onto Tensor Cores. Subsequently, ConvStencil [10] utilizes *stencil2row* transformations and *dual tessellation* to further optimize this adaptation, while SPIDER [16] introduces *Strided Swapping* to further enable sparse ALUs with higher compute throughput. As illustrated in Figure 2, these approaches outperform CUDA Core implementation, DRStencil, by 1.48 \times , 2.23 \times , and 4.60 \times , respectively. This presents a fundamental paradox: Tensor Cores deliver substantial performance gains for stencils, contradicting the long-standing consensus that they are not suitable for these memory-bound tasks.

The aforementioned paradox raises a critical research question: **Why Tensor Cores benefit stencil computation, a problem conventionally recognized as memory-bound? And what is the underlying mechanism defying the memory wall?**

To answer these questions, this paper presents an in-depth performance analysis that demystifies the acceleration mechanism of Tensor Cores for stencil computations. By revisiting the interplay between stencil characteristics and Tensor Core constraints,

we characterize the algorithmic inefficiencies and establish an enhanced roofline model to estimate the stencil performance on different hardware units. This model guides a systematic analysis to delineate the *sweet spot* where Tensor Cores outperform general-purpose units. Ultimately, our analysis resolves the initial contradiction by demonstrating that Tensor Cores can indeed *break the performance ceiling* of conventional approaches in certain scenarios.

In summary, this paper makes the following contributions:

- We dissect the architectural mismatches between stencil patterns and Tensor Core constraints, specifically analyzing the performance impact of using Tensor Cores, including overheads from operand alignment and kernel fusion.
- An enhanced performance model that integrates these overheads is proposed to formulate stencil workloads, enabling a fair comparison of effective throughput between Tensor Cores and conventional CUDA Cores.
- We derive analytical criteria to identify the *sweet spot* where Tensor Core acceleration is theoretically profitable, and further demonstrate how Sparse Tensor Cores expand this effective design space.
- We validate our model through extensive evaluations across SOTA implementations, including DRStencil, EBISU, ConvStencil, and SPIDER, validating the effectiveness of our performance model and analytical criteria.

2 What Happened When Introducing Tensor Cores?

To resolve the aforementioned contradiction, we must first understand how stencil computations are adapted onto Tensor Cores. Since Tensor Cores are designed for matrix multiplication, a workload distinct from stencil computation, adapting stencils onto these units is non-trivial. It requires transformations to satisfy constraints regarding tensor contraction and operand size. These transformations, while enabling execution, often introduce additional overheads. This section clarifies these hardware constraints, the corresponding transformations, and the associated overheads.

Symbol	Description
d	Dimensionality of Stencil Pattern.
r	Radius (or Order) of Stencil Pattern.
P	Peak Performance of Specific Hardware.
B	Memory Bandwidth of Specific Hardware.
t	Fusion Depth.
C	Computational Workload.
M	Memory Traffic.
I	Arithmetic Intensity.
K	Number of Points in the Stencil Kernel.
P	Attainable Performance.
S	Sparsity Introduced by Algorithmic Transformation.
α	Redundancy Factor Introduced by Kernel Fusion.

Table 1: Nomenclature.

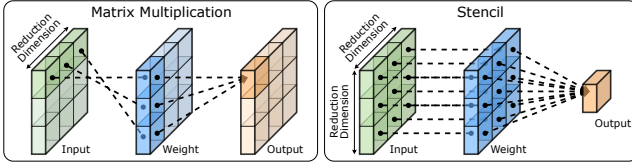


Figure 3: Reduction Dimension Mismatch between Matrix Multiplication and Stencil.

2.1 Constraints Imposed by Tensor Cores

2.1.1 Tensor Contraction Constraint. Tensor Cores are specialized 2D ALUs introduced by NVIDIA to accelerate matrix multiply-and-accumulate (MMA) operations [1]. Similar ALUs have been adopted by other vendors, including AMD’s Matrix Cores [2] and Intel’s Advanced Matrix Extensions (AMX) [3]. Despite minor architectural differences, these units implement the same tensor contraction: $\mathbb{R}^{m \times k} \times \mathbb{R}^{k \times n} \rightarrow \mathbb{R}^{m \times n}$, which can be formalized as:

$$D_{m \times n} = A_{m \times k} \times B_{k \times n} + C_{m \times n}. \quad (1)$$

This operation is often denoted as $mMnNkK$, where each dimension is followed by its size parameter. For example, $m16n8k16$ represents an MMA operation with dimensions $m = 16$, $n = 8$, $k = 16$.

2.1.2 Operand Size Constraint. Unlike conventional ALUs, such as CUDA Cores, which operate on calculations with fine-grained threads, Tensor Cores operate at a coarser granularity. They process fixed-size matrix tiles collectively across a group of threads (e.g., warp). Specifically, modern GPUs define fundamental MMA instruction shapes, the minimum atomic units of computation, including $m8n8k4$ for double, $m16n8k16$ for float [4]. Matrices smaller than these primitive dimensions must be padded or restructured to conform to hardware requirements, often incurring non-negligible overheads in both memory footprint and computational efficiency.

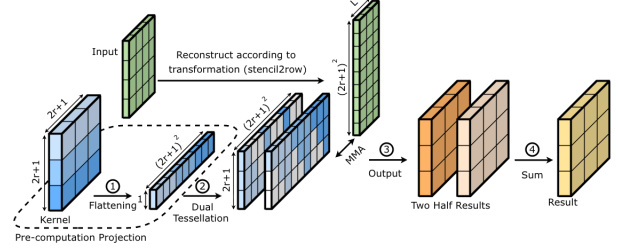
2.2 Adapting Stencil onto Tensor Cores

2.2.1 Bridging Tensor Contraction Mismatch. As described above, Tensor Cores perform matrix multiplication by contracting tensors along a single shared reduction dimension. In contrast, stencil computations involve localized contractions along multiple dimensions, determined by the dimensionality d . Figure 3 shows this structural mismatch between matrix multiplication and Box2D stencil.

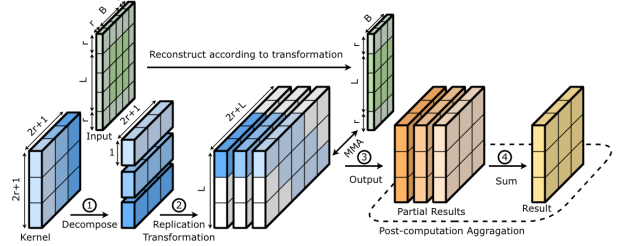
To reconcile this mismatch, prior works have proposed various transformation strategies, which generally fall into two categories:

(1) **Flattening:** As shown in the step ① of Figure 4a, this approach transforms the kernel via flattening. The multi-dimensional stencil weights are linearized along the MMA reduction dimension (similar to `img2col` algorithm). By performing this projection before invoking Tensor Cores, it maps all spatial reduction dimensions onto the single GEMM reduction axis, enabling the Tensor Core to perform the contraction atomically. ConvStencil [10] is a representative work employing this approach.

(2) **Decomposing:** As illustrated in the step ① of Figure 4b, this approach transforms the kernel via decomposition. The stencil kernel is split into multiple independent vectors aligned with the reduction dimensions of Tensor Cores. The partial results generated



(a) Flattening-based Transformation Scheme



(b) Decomposing-based Transformation Scheme

Figure 4: Two Typical Transformation Schemes to Adapt Stencil Computation onto Tensor Cores.

from each vector are subsequently accumulated in Step ④. This post-computation aggregation enables Tensor Cores to complete the full stencil contraction. Representative works employing this approach include TCStencil [29], LoRAStencil [49] and SPIDER [16].

2.2.2 Aligning with Operand Size Requirement. Satisfying the contraction constraint is necessary but insufficient. While the strategies in Step ① successfully transform the computation to MMA form, they typically yield vectors with a dimension of $m = 1$.

This creates a severe conflict with the hardware’s operand size constraint. As noted in §2.1.2, Tensor Cores impose a minimum operand height requirement (e.g., $m = 8$ for $m8n8k4$), directly using these vectors results in extreme under-utilization (e.g., utilizing only $1/8 = 12.5\%$ of compute resource).

To mitigate this, recent methods all employ an additional transformation, such as *dual tessellation* in ConvStencil (step ② in Figure 4a) and *replication* in SPIDER (step ② in Figure 4b). These transformations expand single vectors into matrices that satisfy the minimum operand size requirement.

However, this transformation comes at a cost. As illustrated in Figure 5, constructing these matrices from the original stencil kernel inevitably requires padding with zeros to maintain mathematical equivalence. These padded values introduce redundant operations that do not contribute to the actual computation. We characterize this phenomenon as *sparse redundancy*, where the hardware operates on sparse matrices, thus wasting compute resource.

Notation. To quantify this overhead, let C denote the number of actual operations for stencil computation (excluding padding), and $\mathbb{S} \in (0, 1]$ denote the *sparsity factor* of the transformed matrix (fraction of non-zero elements). The number of operations executed

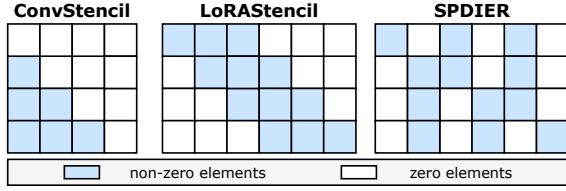


Figure 5: Transformed Sparse Matrices in Recent Tensor Core-based Implementations.

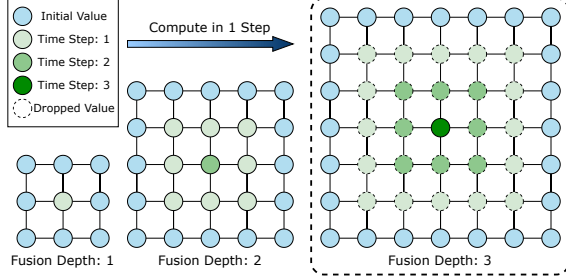


Figure 6: Illustration of Kernel Fusion Strategy for Stencil Computations on Tensor Cores.

on Tensor Cores C_{TC} (TC is short for Tensor Core) is:

$$C_{TC} = \frac{C}{\mathbb{S}} \quad (2)$$

For example, if 50% of the transformed matrix is zero, the executed operations are twice the ideal workload.

2.2.3 Handling Stencils with Small Radius. The aforementioned adaptations enable Tensor Cores to compute stencil problems efficiently for most cases. However, this efficiency degrades significantly for small-radius stencils. To be specific, for the flattening scheme, a small radius $r = 1$ produces a transformed matrix of dimensions $m = 3, n = 9$. To satisfy the operand size constraint (e.g., $m \geq 8$), the dimension m must be padded, wasting 62.5% of compute resource. The decomposition scheme suffers from similar limitations, as the sparsity factor \mathbb{S} increases with the growth of stencil radius r . This implies that a small radius yields excessively sparse matrices. For example, with $r = 1$, about 62.5% of matrix entries are zero-padded values.

To mitigate this inefficiency, recent works adopt a kernel fusion technique to aggregate multiple time steps into a single monolithic step, thereby increasing the stencil kernel size. While conceptually similar to temporal fusion, the underlying execution mechanisms diverge fundamentally.

Specifically, conventional temporal fusion on CUDA Cores processes time steps sequentially, allowing for the explicit reuse of intermediate results. In contrast, Tensor Core-based kernel fusion encapsulates all time steps into a single monolithic matrix operation. This design precludes the reuse of intermediate values, inevitably leading to redundant arithmetic operations. Consequently, while this strategy resolves the operand size mismatch, it introduces a new source of overhead, which we characterize as *fusion redundancy*.

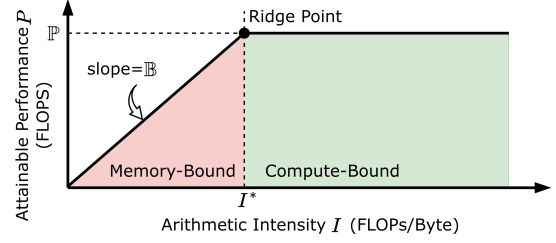


Figure 7: Roofline Model Illustration.

Figure 6 illustrates this effect for a **Box-2D1R** stencil with a fusion depth of 3. The fused kernel operates on a 7×7 spatial points, requiring 49 multiply-and-add operations to produce the central output in a single step. In contrast, a sequentially executed implementation would conduct 3×3 operations updating each step, requiring only 27 operations in total for 3 updates. Thus, kernel fusion introduces 22 redundant operations per output point.

Notation. We characterize this overhead by introducing a *fusion redundancy factor* α (formally derived in §3.2.3), which captures the increase in compute operations due to kernel fusion. The computational workload on Tensor Cores with t fusion steps becomes:

$$C_{TC}^{(t)} = \frac{\alpha}{\mathbb{S}} \cdot C^{(t)} \quad (3)$$

3 Performance Formulation

In this section, we formulate an analytical performance model for stencil computations on both CUDA Cores and Tensor Cores, aiming to characterize their distinct execution behaviors across different hardware.

3.1 Roofline Model

The roofline model serves as a canonical framework for projecting the upper-bound performance of a specific workload [42]. It characterizes the attainable performance P (in FLOPS) as a function of arithmetic intensity I (in FLOPs/Byte), which represents the ratio of computational operations C (in FLOPs) to data traffic M (in Bytes):

$$I = \frac{C}{M} \quad (4)$$

As illustrated in Figure 7, the model establishes a performance roofline comprising two distinct regions, delineated by the ridge point I^* . In the memory-bound region ($I < I^*$), performance scales linearly with arithmetic intensity, with the slope determined by the memory bandwidth \mathbb{B} of the hardware (in Bytes/sec). Conversely, in the compute-bound region ($I > I^*$), performance is throttled by the peak compute throughput \mathbb{P} of the hardware (in FLOPS). Thus, the attainable performance P is formulated as:

$$P = \min(\mathbb{P}, \mathbb{B} \cdot I) \quad (5)$$

This framework provides a rigorous metric to diagnose performance bottlenecks, enabling us to identify whether an implementation is limited by memory bandwidth or compute resource.

3.2 Performance on Different Hardware

3.2.1 Original Stencil Problem. We begin by modeling the performance of the original stencil problem. Let K denote the number of spatial points in the stencil pattern. For example, a box-shaped stencil with dimensionality d and radius r should have $K = (2r+1)^d$ neighboring points.

Each output point is updated via a fused multiply-add (FMA) operation per neighboring point, which corresponds to two floating-point operations (one multiply and one add). Thus, the total number of floating-point operations required to update a single point can be expressed as $C = 2K$.

Regarding memory traffic, let D represent the size (in Bytes) of the data type (e.g., $D = 4$ for float). In an ideal implementation, each update reads one input value and writes one output value, resulting in a total memory traffic of $M = 2D$ bytes per point.

The arithmetic intensity I of this problem is therefore:

$$I = \frac{C}{M} = \frac{K}{D} \quad (6)$$

Finally, the attainable performance P is bounded by both the peak compute throughput \mathbb{P} and the memory bandwidth \mathbb{B} , yielding:

$$P = \min(\mathbb{P}, \mathbb{B} \cdot I), \quad I = \frac{C}{M} = \frac{K}{D} \quad (7)$$

It should be noted that, when implementing stencil computations on GPUs, halo regions may overlap across adjacent tiling blocks. For conciseness, we omit the additional memory accesses and redundant computations incurred by these overlapping elements in our model.

3.2.2 CUDA Core Implementation with Temporal Fusion. The CUDA Core implementation follows the original problem formulation, with computational cost $C_{CU} = C$ and memory traffic $M_{CU} = M$ per output point, where CU is short for CUDA Cores.

To improve performance, temporal fusion is commonly employed to enhance data locality. By fusing t time steps into a single step, the computational workload is increased by a factor of t , yielding $C_{CU}^{(t)} = tC$. Crucially, the intermediate result from earlier steps can be retained in fast on-chip memory (e.g., shared memory or registers), thereby avoiding additional off-chip memory traffic. As a result, the memory traffic remains $M_{CU}^{(t)} = M$.

Consequently, the arithmetic intensity and attainable performance for temporally fused CUDA Core implementation with fusion depth t are given by:

$$I_{CU}^{(t)} = \frac{C_{CU}^{(t)}}{M_{CU}^{(t)}} = t \cdot \frac{K}{D} \quad (8)$$

$$P_{CU}^{(t)} = \min(\mathbb{P}_{CU}, \mathbb{B} \cdot I_{CU}^{(t)})$$

where \mathbb{P}_{CU} denotes the peak compute throughput of the CUDA Core hardware.

3.2.3 Tensor Core Implementation with Kernel Fusion. When adapting stencil computation onto Tensor Cores, the memory traffic per output point remains unchanged, with $M_{TC}^{(t)} = M$. However, the computational workload is significantly affected by two key factors introduced during adaptation: sparsity factor \mathbb{S} and redundancy factor α , as characterized in Equation 3.

Here, the sparsity factor \mathbb{S} arises from hardware-imposed operand size constraints. Being a transformation-specific constant, \mathbb{S} lacks a universal formulation, instead, it must be derived individually based on the underlying transformation scheme.

Meanwhile, the redundancy factor α stems from kernel fusion. It quantifies the inflation in the number of spatial points due to fusing t time steps into a single monolithic kernel, which can be derived as:

$$\alpha = \frac{K^{(t)}}{t \cdot K} \quad (9)$$

where $K^{(t)}$ denotes the number of spatial points in the enlarged stencil kernel after fusion. Fusing t time steps expands the effective stencil radius from r to $t \cdot r$, and the exact form of α depends on the stencil shape.

As an example, consider a box-shaped stencil in d dimensions, the number of kernel points is $K = (2r+1)^d$, while the fused kernel spans $K^{(t)} = (2r \cdot t + 1)^d$. Thus, the redundancy factor becomes:

$$\alpha_{\text{box}} = \frac{K^{(t)}}{tK} = \frac{(2r \cdot t + 1)^d}{t \cdot (2r + 1)^d} \quad (10)$$

Let \mathbb{P}_{TC} denote the peak compute throughput of the Tensor Core hardware. The arithmetic intensity $I_{TC}^{(t)}$ and raw performance of the fused Tensor Core implementation $P_{TC}^{(t)}$ are given by:

$$I_{TC}^{(t)} = \frac{C_{TC}^{(t)}}{M_{TC}^{(t)}} = t \cdot \frac{\alpha}{\mathbb{S}} \cdot \frac{K}{D} \quad (11)$$

$$P_{TC}^{(t)} = \min(\mathbb{P}_{TC}, \mathbb{B} \cdot I_{TC}^{(t)})$$

Importantly, the performance $P_{TC}^{(t)}$ takes every operation into account, including the redundant ones (computing on padded values). Therefore, we must normalize this performance to get the actual performance $P_{TC,actual}^{(t)}$, yielding:

$$I_{TC}^{(t)} = \frac{C_{TC}^{(t)}}{M_{TC}^{(t)}} = t \cdot \frac{\alpha}{\mathbb{S}} \cdot \frac{K}{D} \quad (12)$$

$$P_{TC,actual}^{(t)} = \frac{P_{TC}^{(t)}}{\frac{\alpha}{\mathbb{S}}} = \frac{\mathbb{S}}{\alpha} \cdot \min(\mathbb{P}_{TC}, \mathbb{B} \cdot I_{TC}^{(t)})$$

4 How Can Tensor Cores Accelerate Stencil?

4.1 Performance Comparative Analysis

With the performance model established, we assess the acceleration potential of Tensor Cores for stencil computations by comparing their effective performance $P_{TC,actual}^{(t)}$ against the baseline CUDA Cores $P_{CU,actual}^{(t)}$. Since CUDA Cores execution incurs no computational redundancy, its effective performance $P_{CU,actual}^{(t)}$ aligns directly with its theoretical throughput $P_{CU}^{(t)}$. Leveraging Equation 8 and Equation 12, we formulate the speedup ratio as:

$$\begin{aligned} \frac{P_{TC,actual}^{(t)}}{P_{CU,actual}^{(t)}} &= \frac{\frac{\mathbb{S}}{\alpha} \cdot \min(\mathbb{P}_{TC}, \mathbb{B} \cdot I_{TC}^{(t)})}{\min(\mathbb{P}_{CU}, \mathbb{B} \cdot I_{CU}^{(t)})} \\ &= \frac{\frac{\mathbb{S}}{\alpha} \cdot \min(\mathbb{P}_{TC}, \mathbb{B} \cdot t \cdot \frac{\alpha}{\mathbb{S}} \cdot \frac{K}{D})}{\min(\mathbb{P}_{CU}, \mathbb{B} \cdot t \cdot \frac{K}{D})} \end{aligned} \quad (13)$$

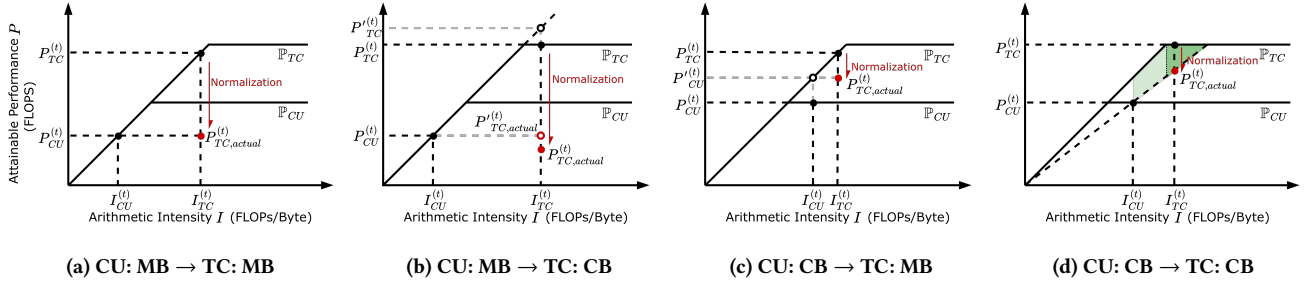


Figure 8: Illustration of Stencil Performance on CUDA Cores and Tensor Cores under Four Scenarios. *MB* denotes memory-bound problems and *CB* represents compute-bound problems.

This ratio reflects the speedup of adapting stencils onto Tensor Cores compared to conventional CUDA Core implementations. A ratio exceeding 1 indicates that Tensor Cores deliver effective acceleration.

Given the piecewise nature of the underlying performance models, we linearize the performance model to rigorously evaluate it by partitioning our analysis into four orthogonal scenarios. These scenarios are strictly defined by the memory-bound and compute-bound states of the comparison units.

(1) Memory-bound on CUDA Cores → Memory-bound on Tensor Cores.

When both implementations operate within the memory-bound region, the peak throughput is strictly throttled by the memory bandwidth \mathbb{B} . The performance ratio simplifies to:

$$\frac{P_{TC,actual}^{(t)}}{P_{CU,actual}^{(t)}} = \frac{\frac{\mathbb{S}}{\alpha} \cdot \mathbb{B} \cdot t \cdot \frac{\alpha}{\mathbb{S}} \cdot \frac{K}{D}}{\mathbb{B} \cdot t \cdot \frac{K}{D}} = 1 \quad (14)$$

This indicates that the effective stencil performance is **equivalent** on both CUDA Cores and Tensor Cores under the memory-bandwidth constraints. As illustrated in Figure 8a, the superior throughput provided by Tensor Cores is entirely offset by the overhead of processing redundant zero-padded elements.

(2) Memory-bound on CUDA Cores → Compute-bound on Tensor Cores.

In this scenario, the CUDA Core baseline is memory-bound. Conversely, the transformations required for Tensor Cores inflate the arithmetic intensity, driven by sparsity and redundancy factors, thereby shifting the execution into the compute-bound region. Consequently, the speedup ratio is derived as:

$$\frac{P_{TC,actual}^{(t)}}{P_{CU,actual}^{(t)}} = \frac{\frac{\mathbb{S}}{\alpha} \cdot \mathbb{P}_{TC}}{\mathbb{B} \cdot t \cdot \frac{K}{D}} \quad (15)$$

Under this scenario ($\mathbb{P}_{TC} < \mathbb{B} \cdot I_{TC}^{(t)}$), the Tensor Core implementation is limited by compute resource, implying that:

$$\frac{P_{TC,actual}^{(t)}}{P_{CU,actual}^{(t)}} = \frac{\frac{\mathbb{S}}{\alpha} \cdot \mathbb{B} \cdot I_{TC}^{(t)}}{\mathbb{B} \cdot t \cdot \frac{K}{D}} < \frac{\frac{\mathbb{S}}{\alpha} \cdot \mathbb{B} \cdot t \cdot \frac{\alpha}{\mathbb{S}} \cdot \frac{K}{D}}{\mathbb{B} \cdot t \cdot \frac{K}{D}} = 1 \quad (16)$$

As a result, Tensor Core implementation consistently **underperforms** CUDA Core implementation in this scenario. As illustrated in Figure 8b, achieving equivalent stencil performance on CUDA

Cores would necessitate a theoretical throughput of $P'_{TC}^{(t)}$ on Tensor Cores, a value that exceeds the physical hardware ceiling. Consequently, the effective performance on Tensor Cores is penalized by this computational limit, failing to match the performance on CUDA Cores.

(3) Compute-bound on CUDA Cores → Memory-bound on Tensor Cores.

Although adapting stencils to Tensor Cores increases arithmetic intensity, the workload may paradoxically shift from compute-bound to memory-bound. This occurs because the higher peak throughput of Tensor Cores \mathbb{P}_{TC} moves the ridge point significantly to the right, making it harder to saturate compute resource. Under the condition $I_{CU}^* < I_{TC}^{(t)} < I_{TC}^{(t)} < I_{TC}^*$, the workload becomes memory-bound, and the performance ratio is formulated as:

$$\begin{aligned} \frac{P_{TC,actual}^{(t)}}{P_{CU,actual}^{(t)}} &= \frac{\frac{\mathbb{S}}{\alpha} \cdot \mathbb{B} \cdot t \cdot \frac{\alpha}{\mathbb{S}} \cdot \frac{K}{D}}{\mathbb{P}_{CU}} \\ &> \frac{\frac{\mathbb{S}}{\alpha} \cdot \mathbb{B} \cdot t \cdot \frac{\alpha}{\mathbb{S}} \cdot \frac{K}{D}}{\mathbb{B} \cdot t \cdot \frac{K}{D}} \\ &= 1 \end{aligned} \quad (17)$$

This scenario highlights where Tensor Cores consistently **outperform** the baseline. Figure 8c illustrates that the effective stencil performance on Tensor Cores reaches the hypothetical throughput of CUDA Cores with unlimited compute resource $P'_{CU}^{(t)}$. In effect, introducing Tensor Cores in this scenario *breaks the performance ceiling* of CUDA Cores.

(4) Compute-bound on CUDA Cores → Compute-bound on Tensor Cores.

When implementations on both units are compute-bound, performance no longer scales with arithmetic intensity. Instead, the attainable throughput is limited by the peak compute throughput of the respective execution units. The ratio is given by:

$$\frac{P_{TC,actual}^{(t)}}{P_{CU,actual}^{(t)}} = \frac{\frac{\mathbb{S}}{\alpha} \cdot \mathbb{P}_{TC}}{\mathbb{P}_{CU}} \quad (18)$$

In this scenario, acceleration is **conditional rather than guaranteed**. Achieving performance gains requires a speedup ratio greater than 1. Since the hardware peak performances \mathbb{P}_{CU} , \mathbb{P}_{TC} and sparse factor \mathbb{S} are fixed for a given transformation on a specific

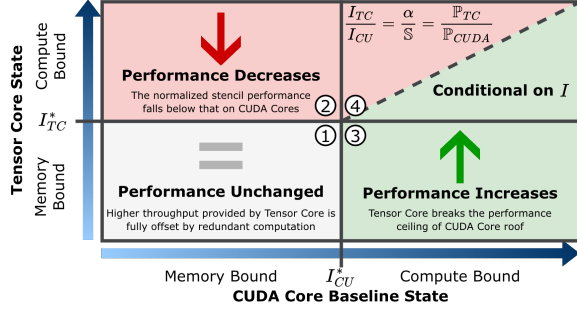


Figure 9: Illustration of Performance Criteria Utilizing Tensor Cores for Stencil Computations.

hardware, the redundancy factor α becomes the decisive determinant. Consequently, effective acceleration necessitates:

$$\alpha < \mathbb{S} \cdot \frac{P_{TC}}{P_{CU}} \quad (19)$$

As formalized in Equation 9, α increases with the growth of fusion depth t . Taking the box-shaped stencil defined in Equation 10 as an example, the redundancy factor is $\alpha_{\text{box}} = \frac{(2r-t+1)^d}{t \cdot (2r+1)^d}$, exhibiting a polynomial growth rate of $O(t^{(d-1)})$. This scaling behavior implies that an aggressive fusion strategy rapidly inflates the redundancy factor α , thereby diminishing the effective acceleration provided by Tensor Cores. Consequently, a careful selection of the fusion step t is critical.

Moreover, leveraging the arithmetic intensity definitions in Equation 8 and Equation 12, the scaling factor $\frac{\mathbb{S}}{\alpha}$ can be reformulated as $\frac{I_{CU}^{(t)}}{I_{TC}^{(t)}}$. This leads to the relationship $P_{TC, \text{actual}}^{(t)} = \frac{I_{CU}^{(t)}}{I_{TC}^{(t)}} \cdot P_{TC}^{(t)}$. Graphically, this condition delineates the profitable region, illustrated in dark green in Figure 8d. The union of this area and the light green region from Scenario 3 collectively defines the *sweet spot* for Tensor Core acceleration.

Summary. Tensor Cores can indeed accelerate stencil computations, but their effectiveness is conditional. Figure 9 synthesizes the performance implications across four scenarios, offering a unified framework that resolves the apparent contradiction highlighted in § 1. Specifically, the figure (Scenarios 1 and 2) illustrates that when the stencil computation is memory-bound on CUDA Cores, utilizing Tensor Cores yields no benefit or even degrades performance. This observation provides a theoretical basis for the conventional view that Tensor Cores are not suited for stencils. Conversely, Scenarios 3 and 4 demonstrate that for compute-bound stencils, Tensor Cores unlock substantial performance gains, particularly within the *sweet spot* (green region). This finding validates the empirical success reported in prior works such as TCStencil and ConvStencil. Ultimately, our model bridges the gap between conventional wisdom and recent empirical breakthroughs.

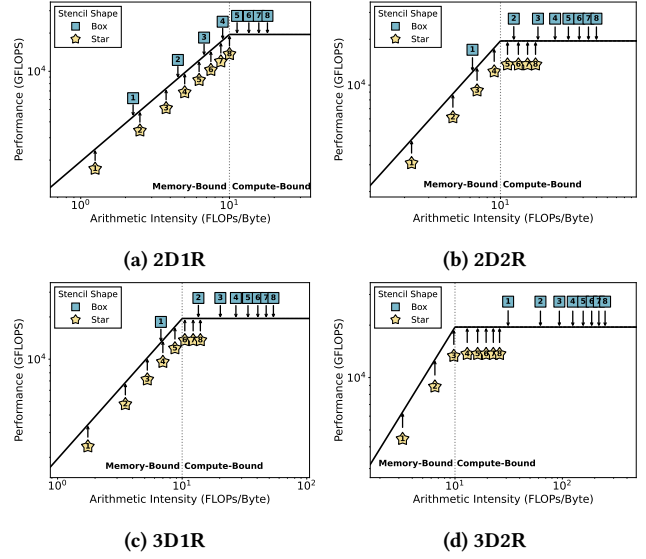


Figure 10: Problem Classification for Various Stencil Configurations on NVIDIA A100 GPU with Float Precision. The number in the marker denotes the temporal fuse steps.

4.2 Stencil is NOT Always Memory-Bound

We have demonstrated that Tensor Cores provide performance boosts primarily when the workload saturates the compute resource of CUDA Cores (i.e., *sweet spot*). While naive stencil computations typically exhibit low arithmetic intensity, techniques such as temporal fusion are widely adopted to alleviate memory pressure. Consequently, optimized stencil implementations frequently transition into the compute-bound region, depending on factors such as stencil shape, data type, fusion depth, and hardware specifications.

Motivated by this insight, we examine whether temporally fused stencil kernels have sufficient arithmetic intensity to benefit from Tensor Core acceleration. Our investigation proceeds in two phases: first, we employ theoretical analysis to identify the bottleneck migration; second, we verify these predictions with empirical results.

By applying Equation 8, we compare the theoretical arithmetic intensity of various representative stencil configurations against hardware limits, as shown in Figure 10. Our analysis reveals a clear trend: most stencil problems transition into a compute-bound region after applying sufficient temporal fusion. Generally, kernels with higher dimensionality or larger stencil radius require fewer fusion steps to reach this transition. Notably, inherently intensive kernels, such as the Box-3D2R, operate in the compute-bound region even without fusion.

Our empirical validation leverages EBISU [48], a representative SOTA stencil framework. We conduct profiling on an NVIDIA A100 GPU, covering star- and box-shaped stencils (float and double) across fusion depths from 1 to 8. Consistent with our theoretical analysis, the results demonstrate that sufficient fusion depth shifts stencils into the compute-bound region. For instance, box stencils transition at $t = 3$, while star stencils, with lower inherent intensity, transition at $t = 5$.

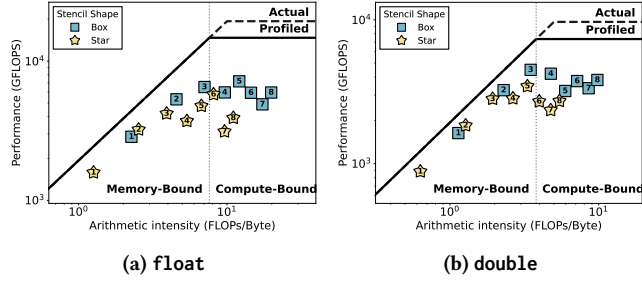


Figure 11: The Roofline Chart Profiled from EBISU Implementation for 2D Stencil with Radius $r = 1$ on A100 GPU. The number in the marker denotes the temporal fuse steps.

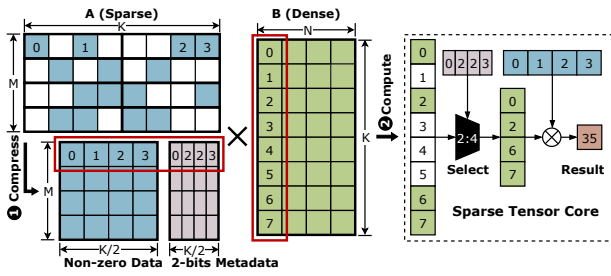


Figure 12: 2:4 Structured Sparse Format and its Compressed Representation for Sparse Tensor Cores.

It is worth noting that the empirically observed transition points appear slightly earlier than theoretical predictions. This discrepancy arises because the GPU clock is locked at a lower frequency during profiling to ensure stability and reproducibility of the results. This frequency locking lowers the effective compute ceiling, as reflected in Figure 10, thereby allowing the kernel to saturate compute resource at a shallower fusion depth. When using the actual peak performance, the theoretical and empirical transition points align closely.

These results effectively refute the prevailing belief that stencil computations are universally memory-bound. On the contrary, we demonstrate that SOTA stencil implementations, especially those leveraging temporal fusion, routinely saturate the compute resource of modern GPUs. This paradigm shift presents a compelling opportunity to harness Tensor Cores, utilizing their superior throughput to push performance further. This insight aligns with both the performance trends observed in recent studies and our analytical derivations in §4.1.

4.3 Further Acceleration with Sparse Hardware

As discussed in §2.2.2, adapting stencil computations to Tensor Cores necessitates zero-padding to satisfy fixed operand size constraints. This introduces computational redundancy, as operations on padded zeros do not contribute to the final result. Fortunately, modern GPU architectures have augmented their matrix ALUs with native hardware support for sparsity. By skipping operations on zero-valued elements, the effective compute throughput can be significantly improved.

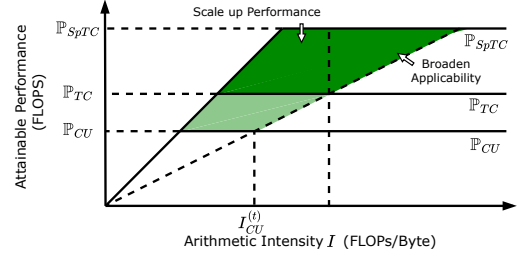


Figure 13: Sweet Spot for SpTC Acceleration.

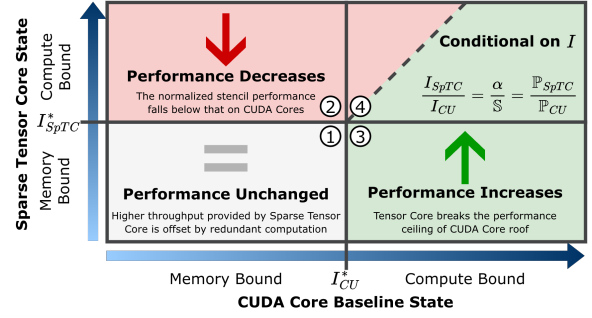


Figure 14: Illustration of Performance Criteria Utilizing Sparse Tensor Cores for Stencil Computations.

Specifically, NVIDIA integrates Sparse Tensor Cores (SpTCs) [1] to accelerate sparse matrix operations. SpTCs rely on a 2:4 structured sparsity constraint (Figure 12), where each block of four elements contains a maximum of two non-zeros. This structure permits a compressed representation comprising packed values and 2-bit positional metadata. By skipping invalid elements based on this metadata, SpTCs deliver a 2 \times speedup compared to their dense counterparts. To leverage this throughput for stencil computations, recent studies like SparStencil [28] and SPIDER [16] employ methods such as *Strided Swapping* to adapt kernels into SpTC-compatible formats.

Adapting onto SpTC leaves the theoretical arithmetic intensity (Equation 12) unchanged ($I_{SpTC}^{(t)} = I_{TC}^{(t)}$). Letting \mathbb{P}_{SpTC} denote the peak throughput of SpTC, the resulting performance model is expressed as:

$$I_{SpTC}^{(t)} = t \cdot \frac{\alpha}{\mathbb{S}} \cdot \frac{K}{D}$$

$$P_{SpTC}^{(t)} = \min(\mathbb{P}_{SpTC}, \mathbb{B} \cdot I_{SpTC}^{(t)}) \quad (20)$$

$$P_{SpTC,actual}^{(t)} = \frac{\mathbb{S}}{\alpha} \min(\mathbb{P}_{SpTC}, \mathbb{B} \cdot I_{SpTC}^{(t)})$$

Leveraging SpTCs yields a twofold benefit. First, it boosts the peak throughput for existing compute-bound workloads. By raising the hardware ceiling from \mathbb{P}_{TC} to \mathbb{P}_{SpTC} , SpTCs directly scale up the performance of stencils that are already optimized on Tensor Cores, as shown in Figure 13. Second, it broadens the applicability of Tensor Core acceleration. On dense Tensor Cores, the throughput gain for stencils with aggressive temporal fusion is often offset

by the overhead of redundant computations ($\frac{\alpha}{\mathbb{S}}$), rendering them slower than CUDA Core baselines. SpTCs mitigate this issue: their 2 \times throughput is sufficient to amortize the redundancy, converting previously inefficient configurations into viable candidates for acceleration. This effectively expands the *sweet spot* for specialized hardware, as demonstrated in Figure 14.

5 Evaluation

5.1 Evaluation Setup

Platforms. Our evaluation platform utilizes two Intel Xeon Platinum 8558P CPUs, 512GB DDR5 memory, and NVIDIA A100-80GB PCIe GPU. The system operates on Ubuntu 22.04 LTS with CUDA 12.8 and cuDNN 9.8.0.

Baselines. In this section, we consider a comprehensive set of baselines, including cuDNN [11], DRStencil [45] and EBISU [48] for CUDA Core architectures, as well as TCStencil [29], ConvStencil [10], LoRAStencil [49] and SPIDER [16] for Tensor Core architectures.

To verify the correctness of our performance formulation and analytical criteria, we specifically select SOTA implementations on CUDA Cores (EBISU), Tensor Cores (ConvStencil and SPIDER) as representative methods. This selection is grounded in the performance analysis presented in §5.5, where these methods are shown to deliver SOTA performance in their respective categories. By targeting the most competitive implementations, we ensure the rigor and generality of our evaluation.

It should be noted that we adapt the baselines in two aspects. First, we extend the codebases to support unimplemented stencil shapes to enable case-by-case comparison. For instance, we implement Box-2D7R support for EBISU. Second, we unify the handling of stencil kernels to ensure a fair comparison. While some baselines originally compile stencil parameters as constant literals, we modify all implementations to support dynamic kernel values at runtime.

Benchmarks. We evaluate our approach using various stencil shapes ranging from 2D to 3D. For 2D stencils, we employ a domain size of 10240×10240 and evaluate both Box and Star shapes (radius $r \in \{1, 3, 7\}$). For 3D stencils, we utilize a domain size of $1024 \times 1024 \times 1024$, covering both Box and Star shapes with $r = 1$. The radius is selected to align with the dimension requirement of Tensor Cores.

5.2 Verification of Proposed Formulations

We assess the accuracy of our model by comparing its analytical predictions with empirical data extracted from NVIDIA Nsight Compute (ncu). Specifically, we estimate the analytical metrics for computation C , memory traffic M , and arithmetic intensity I using Equation 8 and 12. The redundancy factor α is derived from Equation 10, while \mathbb{S} remains constant for each implementation. For validation, we profile the computing kernels using the ncu profiler, correlating *achieved work* and *achieved traffic* with the modeled C and M . A detailed comparison across different baselines and patterns is shown in Table 2.

5.2.1 Memory Traffic Analysis (M). First, we examine the behavior of memory traffic. As detailed in Table 2, the experimental values for

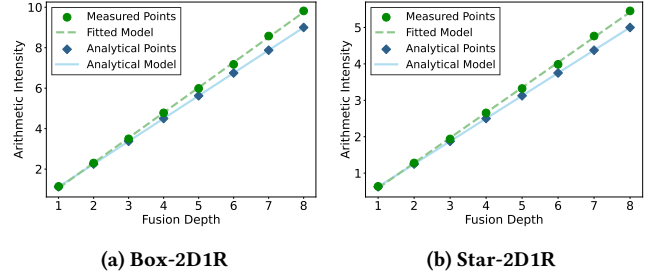


Figure 15: Arithmetic Intensity vs. Fusion Depth for CUDA Core Implementation with Double Precision.

M remain nearly constant across varying temporal fusion depth t . For instance, in the EBISU baseline, comparing the data in Rows 1 and 2 (as well as Rows 3 and 4) reveals that increasing t induces negligible fluctuations in memory traffic. The experimental results confirm that global memory traffic is dominated by compulsory data movement, as intermediate updates are effectively handled via on-chip memory, thereby decoupling global memory traffic from the temporal depth and validating our formulation.

5.2.2 Computational Operation Analysis (C). In terms of computational operations, our model exhibits high predictive accuracy across different hardware backends. For the CUDA Core-based EBISU, the measured C aligns closely with analytical predictions, confirming the precision of our fundamental operation counting logic. For Tensor Core-based methods (ConvStencil and SPIDER), we further analyze the computational redundancy introduced by hardware adaptation. Comparing Rows 7 and 9 (identical temporal depth t , different \mathbb{S}) confirms that the measured computation scales correctly with our estimated sparsity factor \mathbb{S} . Conversely, fixing \mathbb{S} while varying t (Rows 5 vs. 6, 7 vs. 8, and 9 vs. 10) reveals that the computational overhead follows the redundancy ratio α defined in Equation 10. Collectively, these results show that the total computation volume aligns with Equation 3, proving that our model accurately encapsulates both intrinsic arithmetic and the necessary padding overheads.

5.2.3 Arithmetic Intensity Analysis (I). Finally, we evaluate the arithmetic intensity $I = C/M$ to validate our analytical model. Overall, the experimental results closely match the analytical derivation across both CUDA Core and Tensor Core implementations.

To rigorously verify the correlation between arithmetic intensity and the temporal fusion depth t , we conducted an extensive experiment using the CUDA Core baseline, leveraging its flexibility in the configuration of fusion depth t . As illustrated in Figure 15, the results reveal a clear linear relationship between I and t , providing strong empirical evidence for our performance model.

5.2.4 Summary and Deviation Analysis. The evaluation results confirm that our analytical formulation captures the fundamental performance characteristics of the system, yielding accurate estimation for C , M , and I across a diverse range of configurations. While the overall correlation is strong, we observe minor yet systematic deviations between the modeled and measured data, which reflect specific hardware behaviors excluded from our model.

	Baseline	Stencil Pattern	Fusion Depth	α	\mathbb{S}	Data Type	Analytical			Experimental		
							C	M	I	C (Δ)	M (Δ)	I (Δ)
1	EBISU	Box-2D1R	3	/	/	double	54	16	3.38	55.78 (3.30%)	15.95 (-0.30%)	3.50 (3.61%)
2		Box-2D3R	1	/	/	double	98	16	6.12	100.65 (2.70%)	15.92 (-0.50%)	6.32 (3.21%)
3		Box-2D1R	7	/	/	float	126	8	15.75	137.35 (9.01%)	7.93 (-0.90%)	17.32 (10.00%)
4		Box-2D7R	1	/	/	float	450	8	56.25	484.51 (7.61%)	7.91 (-1.09%)	61.23 (8.85%)
5	ConvStencil	Box-2D1R	3	1.81	0.5	double	196	16	12.25	208.00 (6.12%)	15.91 (-0.56%)	13.07 (6.73%)
6		Box-2D3R	1	1	0.5							
7		Box-2D1R	7	3.57	0.5	float	900	8	112.50	928.00 (3.11%)	8.27 (3.36%)	112.23 (-0.24%)
8		Box-2D7R	1	1	0.5							
9	SPIDER	Box-2D1R	7	3.57	0.47	float	960	8	120.00	960.00 (0.00%)	7.89 (-1.35%)	121.64 (1.37%)
10		Box-2D7R	1	1	0.47							

Table 2: Comparison of Analytical and Experimental Metrics across Different Baselines. For CUDA Core implementation, factor α and \mathbb{S} are not involved in its formulation.

Case	Stencil Pattern	Fuse Depth	Data Type	Baseline	Arithmetic Intensity	Ridge Point	Bottleneck	Performance (GStencils/sec)	Performance Change	Belonging Scenario
❶	Box-2D1R	3	double	EBISU	3.38	5	Memory	260.90	↓	Scenario 2
				ConvStencil	12.25	10	Compute	190.14		
❷	Box-2D3R	1	double	EBISU	6.13	5	Compute	64.05	≈	Scenario 4
				ConvStencil	12.25	10	Compute	63.33		
❸	Box-2D1R	7	float	EBISU	15.75	10	Compute	318.31	↑	Scenario 3
				SPIDER	120.00	161	Memory	1002.94		
❹	Box-2D7R	1	float	EBISU	21.58	10	Compute	50.35	↑	Scenario 3
				SPIDER	120.00	161	Memory	143.28		
❺	Box-3D1R	3	double	EBISU	10.13	5	Compute	37.74	↓	Scenario 4
				ConvStencil	85.75	10	Compute	24.63		
❻	Box-3D1R	7	float	EBISU	47.25	10	Compute	71.23	↓	Scenario 4
				SPIDER	1795.21	161	Compute	51.13		

Table 3: Comparison of Stencil Performance and Bottleneck Transitions across Representative Cases.

Specifically, the measured values for C consistently exceed analytical predictions. We attribute this slight inflation to overheads in specific implementation, primarily the redundant calculations in halo regions arising from thread block overlaps. These operations are captured by the hardware profiler but are excluded from our formulation. Conversely, the measured memory traffic M is generally lower than predicted. This discrepancy arises because our analytical model assumes all data transfers originate from DRAM (compulsory misses). In practice, the L2 cache effectively filters memory requests, serving a portion of accesses and thereby reducing the actual off-chip traffic observed at the memory controller.

5.3 Analytical Criteria Verification

To assess the validity of our proposed criteria, we conducted an analysis of six representative cases (Cases ❶–❻), by comparing the analytical conclusion and the empirical performance. These cases

include all the cases currently available in SOTA stencil computations on Tensor Cores, encompassing the three distinct scenarios analyzed in §4.1. We quantify the performance using GStencils/sec, the de facto standard metric for stencil throughput. The detailed configurations, bottleneck shifts, and performance results are summarized in Table 3.

Memory-bound on CUDA Cores → Compute-bound on Tensor Cores. Case ❶ exemplifies this scenario. In the baseline implementation (EBISU), the performance is constrained by memory bandwidth (memory-bound). However, due to the redundancy factor α and the sparsity in padded matrices \mathbb{S} , the Tensor Core implementation (ConvStencil) is pushed into a compute-bound region.

Our analytical criteria, as derived in Equation 16, predict that for this scenario, the actual performance is penalized by the computational ceiling of Tensor Cores, causing the effective compute

Baseline	Arithmetic Intensity	Ridge Point	Bottleneck	Performance (GStencils/sec)
SPIDER-Dense	120	81	Compute	327.39
SPIDER-Sparse	120	161	Memory	1002.94

Table 4: Comparison between Dense and Sparse Tensor Cores (Box-2D1R with $t=7$ for float precision).

throughput lower than the baseline. Experimental results corroborate this prediction: the introduction of Tensor Cores resulted in a 27.12% performance degradation.

Compute-bound on CUDA Cores \rightarrow Memory-bound on Tensor Cores. Cases ③ and ④ fall into this category. In these cases, the baseline implementation is strictly constrained by the peak floating-point performance of CUDA Cores (P_{CU}), whereas the Tensor Core implementation (SPIDER) successfully alleviates this compute bottleneck.

Analytically, this scenario represents the ideal use case for acceleration, where the introduction of Tensor Cores breaks the computational ceiling of CUDA Cores, thus provides performance benefits, as derived in Equation 17. Empirically, this is confirmed by substantial speedups of 7.73 \times and 6.64 \times for Case ③ and ④, respectively.

Compute-bound on CUDA Cores \rightarrow Compute-bound on Tensor Cores. This scenario is the most intricate one, where performance gains are *conditional rather than guaranteed*, as derived in Equation 18. We use Cases ②, ⑤, and ⑥ to verify if our *sweet spot* formulation accurately delineates the boundary of performance benefits.

For Case ⑤, the redundancy factor is calculated as $\alpha \approx 1.81$. Given the hardware specifications of A100 GPU ($P_{CU} = 9.7$ TFLOPS and $P_{TC} = 19.5$ TFLOPS for double precision), this case fails to satisfy the condition defined in Equation 19 ($\alpha > \mathbb{S} \cdot \frac{P_{TC}}{P_{CU}}$). Consequently, it falls outside the *sweet spot*, resulting in performance degradation. The experimental observation matches our prediction.

Similarly, for Case ⑥, the larger stencil dimension leads to a higher α value, again violating the *sweet spot* condition. Both theoretical analysis and experimental data indicate a performance degradation.

In contrast, Case ② presents a boundary condition. According to Equation 18, the ratio of the Tensor Core performance to the CUDA Core performance approaches 1. This suggests the case lies near the boundary of the *sweet spot*, implying comparable performance between the two implementations. The experimental results confirm this, showing negligible performance difference.

Summary. Collectively, these experiments demonstrate the validity of our analytical model. By accurately predicting positive, negative, and neutral outcomes across diverse scenarios, our criteria prove effective in guiding the selection of the optimal execution unit for stencil computations.

5.4 Benefits from Sparse Tensor Core

To validate the theoretical advantages of sparse hardware detailed in § 4.3, we compare the native SPIDER implementation utilizing Sparse Tensor Cores against its variant employing dense Tensor Cores. Table 4 presents the performance metrics for a Box-2D1R

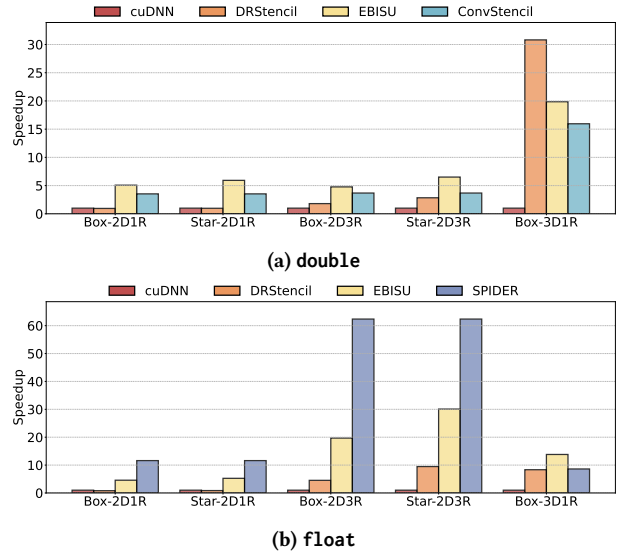


Figure 16: Overall Performance Comparison.

stencil with temporal fusion $t=7$. The results demonstrate that the introduction of SpTCs fundamentally alters the performance bottleneck, transitioning the workload from a compute-bound to a memory-bound region and delivering a remarkable 3.06 \times speedup over the dense baseline. This empirical evidence confirms that the enhanced compute throughput of SpTCs effectively shifts the hardware ridge point and broadens the acceleration scope for stencil computations, thereby elevating the attainable performance.

5.5 Overall Performance Comparison

Finally, we evaluate the overall stencil performance across the different data precisions supported by the baselines. For double precision (double), we benchmark cuDNN, DRStencil, EBISU, and ConvStencil. For single precision (float), we evaluate cuDNN, DRStencil, EBISU, and SPIDER. Two baselines are excluded from this analysis: TCStencil, which is limited to half-precision support, and LoRAStencil, which assumes symmetric stencil kernels and is therefore inapplicable to general-purpose scenarios. As shown in Figure 16, EBISU, ConvStencil, and SPIDER represent the SOTA implementations on CUDA Cores, Tensor Cores, and Sparse Tensor Cores, respectively. These results validate the selection of baselines used for the analysis in our evaluation.

6 Related Work

Traditional Stencil Optimizations on General-Purpose Architectures. Traditional stencil optimizations on CPUs primarily focus on mitigating the memory wall and maximizing data parallelism. Representative optimization techniques, such as tiling [9, 25, 38, 39, 43] and layout transformation [19, 20], are widely employed to enhance data locality. To exploit SIMD capabilities (e.g., AVX, SSE), extensive research has been conducted on both manual [26, 34, 44] and compiler-assisted vectorization [27, 40], aiming to streamline instruction alignment. In the context of GPUs, strategies shift toward hiding memory latency within complex hierarchies. These

include hierarchy-aware tiling [15, 21, 31, 32, 41], temporal blocking via register rotation [13], and optimized prefetching and streaming techniques [17, 35, 36, 50]. However, these approaches are largely bounded by the scalar or vector processing units of traditional architectures.

Stencil Computation on Tensor Cores. Stencil computation has emerged as a critical frontier within this broadening landscape of Tensor Core applications. TCStencil [29] pioneers the stencil-to-GEMM paradigm, reformulating stencil computations as matrix multiplications to unlock Tensor Core throughput. Subsequent works, such as ConvStencil [10] and LoRAStencil [49], refine this transformation to minimize memory overheads. Despite these advances, a fundamental limitation persists: adapting stencils to Tensor Cores inevitably incurs computational redundancy. To address this, FlashFFTStencil [18] leverages FFT to maximize arithmetic intensity. Meanwhile, sparsity-centric approaches like SPIDER [16] and SparStencil [28] employ novel stride-swapping and compilation techniques to align stencil patterns with hardware requirements, exploiting the hardware-intrinsic 2:4 sparsity of Sparse Tensor Cores.

7 Conclusion

This paper resolves the apparent contradiction between the memory-bound nature of stencil computations and their observed acceleration on compute-centric Tensor Cores. By quantifying the algorithmic redundancy and arithmetic intensity shifts, we propose an enhanced performance model that rigorously delineates the *sweet spot* where the benefits of high-throughput units outweigh the costs of adaptation. Our analysis reveals that Tensor Cores become viable when temporal fusion effectively shifts the bottleneck. Extensive evaluations across SOTA implementations like ConvStencil and SPIDER corroborate our model, grounding our analysis in empirical results. Consequently, our work reconciles the discrepancy between conventional assumptions and empirical reality, providing a systematic guideline for stencil acceleration.

References

- [1] 2021. NVIDIA AMPERE GA102 GPU ARCHITECTURE. <https://www.nvidia.com/content/PDF/nvidia-ampere-ga-102-gpu-architecture-whitepaper-v2.pdf>.
- [2] 2025. AMD CDNA™ Architecture. <https://www.amd.com/en/technologies/cdna.html>.
- [3] 2025. Intel Advanced Matrix Extensions. <https://www.intel.cn/content/www/cn/zh/products/docs/accelerator-engines/what-is-intel-amx.html>.
- [4] 2025. Parallel Thread Execution ISA Version 9.1. <https://docs.nvidia.com/cuda/parallel-thread-execution/index.html>.
- [5] Kadir Akbudak, Hatem Ltaief, Vincent Etienne, Rached Abdelkhalak, Thierry Tonellot, and David Keyes. 2020. Asynchronous computations for solving the acoustic wave propagation equation. *The International Journal of High Performance Computing Applications* 34, 4 (2020), 377–393.
- [6] Yulong Ao, Chao Yang, Xinliang Wang, Wei Xue, Haohuan Fu, Fangfang Liu, Lin Gan, Ping Xu, and Wenjing Ma. 2017. 26 pflops stencil computations for atmospheric modeling on sunway taihulight. In *2017 IEEE International Parallel and Distributed Processing Symposium (IPDPS)*. IEEE, 535–544.
- [7] Krste Asanovic, Ras Bodik, Bryan Catanzaro, Joseph Gebis, Parry Husbands, Kurt Keutzer, David Patterson, William Plishker, John Shalf, and Samuel Webb Williams. 2006. The landscape of parallel computing research: A view from Berkeley. (2006).
- [8] Tal Ben-Nun, Linus Groner, Florian Deconinck, Tobias Wicky, Eddie Davis, Johann Dahm, Oliver D Elbert, Rhea George, Jeremy McGibbon, Lukas Trümper, et al. 2022. Productive performance engineering for weather and climate modeling with python. In *SC22: International Conference for High Performance Computing, Networking, Storage and Analysis*. IEEE, 1–14.
- [9] Uday Bondhugula, Vinayaka Bandishti, and Irshad Pananilath. 2016. Diamond tiling: Tiling techniques to maximize parallelism for stencil computations. *IEEE Transactions on Parallel and Distributed Systems* 28, 5 (2016), 1285–1298.
- [10] Yuetao Chen, Kun Li, Yuhao Wang, Donglin Bai, Lei Wang, Lingxiao Ma, Liang Yuan, Yunquan Zhang, Ting Cao, and Mao Yang. 2024. Convstencil: Transform stencil computation to matrix multiplication on tensor cores. In *Proceedings of the 29th ACM SIGPLAN Annual Symposium on Principles and Practice of Parallel Programming*, 333–347.
- [11] Sharan Chetlur, Cliff Woolley, Philippe Vandermersch, Jonathan Cohen, John Tran, Bryan Catanzaro, and Evan Shelhamer. 2014. cudnn: Efficient primitives for deep learning. *arXiv preprint arXiv:1410.0759* (2014).
- [12] Phillip Colella. 2004. Defining Software Requirements for Scientific Computing.
- [13] Thomas L Falch and Anne C Elster. 2014. Register caching for stencil computations on GPUs. In *2014 16th International Symposium on Symbolic and Numeric Algorithms for Scientific Computing*. IEEE, 479–486.
- [14] Matteo Frigo and Volker Strumpen. 2005. Cache oblivious stencil computations. In *Proceedings of the 19th annual international conference on Supercomputing*, 361–366.
- [15] Tobias Grosser, Albert Cohen, Paul HJ Kelly, Jagannathan Ramanujam, Ponuswamy Sadayappan, and Sven Verdoolaege. 2013. Split tiling for GPUs: automatic parallelization using trapezoidal tiles. In *Proceedings of the 6th Workshop on General Purpose Processor Using Graphics Processing Units*, 24–31.
- [16] Qiqi GU, Chenpeng Wu, Heng Shi, and Jianguo Yao. 2025. SPIDER: Unleashing Sparse Tensor Cores for Stencil Computation via Strided Swapping. arXiv:2506.22035 [cs.DC] <https://arxiv.org/abs/2506.22035>
- [17] Tobias Gysi, Christoph Müller, Oleksandr Zinenko, Stephan Herhut, Eddie Davis, Tobias Wicky, Oliver Fuhrer, Torsten Hoefler, and Tobias Grosser. 2021. Domain-specific multi-level ir rewriting for gpu: The open earth compiler for gpu-accelerated climate simulation. *ACM Transactions on Architecture and Code Optimization (TACO)* 18, 4 (2021), 1–23.
- [18] Haozhi Han, Kun Li, Wei Cui, Donglin Bai, Yiwei Zhang, Liang Yuan, Yifeng Chen, Yunquan Zhang, Ting Cao, and Mao Yang. 2025. FlashFFTStencil: Bridging Fast Fourier Transforms to Memory-Efficient Stencil Computations on Tensor Core Units. In *Proceedings of the 30th ACM SIGPLAN Annual Symposium on Principles and Practice of Parallel Programming*, 355–368.
- [19] Tom Henretty, Kevin Stock, Louis-Noël Pouchet, Franz Franchetti, J Ramanujam, and P Sadayappan. 2011. Data layout transformation for stencil computations on short-vector simd architectures. In *Compiler Construction: 20th International Conference, CC 2011, Held as Part of the Joint European Conferences on Theory and Practice of Software, ETAPS 2011, Saarbrücken, Germany, March 26–April 3, 2011. Proceedings 20*. Springer, 225–245.
- [20] Tom Henretty, Richard Veras, Franz Franchetti, Louis-Noël Pouchet, Jagannathan Ramanujam, and Ponnuswamy Sadayappan. 2013. A stencil compiler for short-vector simd architectures. In *Proceedings of the 27th international ACM conference on International conference on supercomputing*, 13–24.
- [21] Justin Holewinski, Louis-Noël Pouchet, and Ponnuswamy Sadayappan. 2012. High-performance code generation for stencil computations on GPU architectures. In *Proceedings of the 26th ACM international conference on Supercomputing*, 311–320.
- [22] Hung T Huynh, Zhi J Wang, and Peter E Vincent. 2014. High-order methods for computational fluid dynamics: A brief review of compact differential formulations on unstructured grids. *Computers & fluids* 98 (2014), 209–220.
- [23] Mathias Jacquelin, Mauricio Araya-Polo, and Jie Meng. 2022. Scalable distributed high-order stencil computations. In *SC22: International Conference for High Performance Computing, Networking, Storage and Analysis*. IEEE, 1–13.
- [24] Byunghyun Jang, Perhaad Mistry, Dana Schaa, Rodrigo Dominguez, and David Kaeli. 2010. Data transformations enabling loop vectorization on multithreaded data parallel architectures. In *Proceedings of the 15th ACM SIGPLAN symposium on Principles and practice of parallel programming*, 353–354.
- [25] Guohua Jin, John Mellor-Crummey, and Robert Fowler. 2001. Increasing temporal locality with skewing and recursive blocking. In *Proceedings of the 2001 ACM/IEEE Conference on Supercomputing*, 43–43.
- [26] Ken Kennedy and John R Allen. 2001. *Optimizing compilers for modern architectures: a dependence-based approach*. Morgan Kaufmann Publishers Inc.
- [27] Mingzhen Li, Yi Liu, Hailong Yang, Yongmin Hu, Qingxiao Sun, Bangduo Chen, Xin You, Xiaoyan Liu, Zhongzhi Luan, and Depei Qian. 2021. Automatic code generation and optimization of large-scale stencil computation on many-core processors. In *Proceedings of the 50th International Conference on Parallel Processing*, 1–12.
- [28] Qi Li, Kun Li, Haozhi Han, Liang Yuan, Yunquan Zhang, Yifeng Chen, Junshi Chen, Hong An, Ting Cao, and Mao Yang. 2025. SparStencil: Retargeting Sparse Tensor Cores to Scientific Stencil Computations via Structured Sparsity Transformation. In *Proceedings of the International Conference for High Performance Computing, Networking, Storage and Analysis*, 1495–1509.
- [29] Xiaoyan Liu, Yi Liu, Hailong Yang, Jianjin Liao, Mingzhen Li, Zhongzhi Luan, and Depei Qian. 2022. Toward accelerated stencil computation by adapting tensor core unit on GPU. In *Proceedings of the 36th ACM International Conference on Supercomputing (Virtual Event) (ICS '22)*. Association for Computing Machinery, New York, NY, USA, Article 28, 12 pages. doi:10.1145/3524059.3532392

- [30] David J Lusher, Satya P Jammy, and Neil D Sandham. 2021. OpenSBLI: Automated code-generation for heterogeneous computing architectures applied to compressible fluid dynamics on structured grids. *Computer Physics Communications* 267 (2021), 108063.
- [31] Naoya Maruyama and Takayuki Aoki. 2014. Optimizing stencil computations for NVIDIA Kepler GPUs. In *Proceedings of the 1st international workshop on high-performance stencil computations*, Vienna. Citeseer, 89–95.
- [32] Anthony Nguyen, Nadathur Satish, Jatin Chhugani, Changkyu Kim, and Pradeep Dubey. 2010. 3.5-D blocking optimization for stencil computations on modern CPUs and GPUs. In *SC'10: Proceedings of the 2010 ACM/IEEE International Conference for High Performance Computing, Networking, Storage and Analysis*. IEEE, 1–13.
- [33] Long Qu, Rached Abdelkhalak, Hatem Ltaief, Issam Said, and David Keyes. 2023. Exploiting temporal data reuse and asynchrony in the reverse time migration. *The International Journal of High Performance Computing Applications* 37, 2 (2023), 132–150.
- [34] Prashant Singh Rawat, Aravind Sukumaran-Rajam, Atanas Rountev, Fabrice Rastello, Louis-Noël Pouchet, and Ponnuswamy Sadayappan. 2018. Associative instruction reordering to alleviate register pressure. In *SC18: International Conference for High Performance Computing, Networking, Storage and Analysis*. IEEE, 590–602.
- [35] Prashant Singh Rawat, Miheer Vaidya, Aravind Sukumaran-Rajam, Mahesh Ravishankar, Vinod Grover, Atanas Rountev, Louis-Noël Pouchet, and Ponnuswamy Sadayappan. 2018. Domain-specific optimization and generation of high-performance GPU code for stencil computations. *Proc. IEEE* 106, 11 (2018), 1902–1920.
- [36] Prashant Singh Rawat, Miheer Vaidya, Aravind Sukumaran-Rajam, Atanas Rountev, Louis-Noël Pouchet, and P Sadayappan. 2019. On optimizing complex stencils on GPUs. In *2019 IEEE International Parallel and Distributed Processing Symposium (IPDPS)*. IEEE, 641–652.
- [37] Gabriel Rivera and Chau-Wen Tseng. 2000. Tiling optimizations for 3D scientific computations. In *SC'00: Proceedings of the 2000 ACM/IEEE Conference on Supercomputing*. IEEE, 32–32.
- [38] Yonghong Song and Zhiyuan Li. 1999. New tiling techniques to improve cache temporal locality. *ACM SIGPLAN Notices* 34, 5 (1999), 215–228.
- [39] Robert Strzodka, Mohammed Shaheen, Dawid Pajak, and Hans-Peter Seidel. 2010. Cache oblivious parallelograms in iterative stencil computations. In *Proceedings of the 24th ACM International Conference on Supercomputing*. 49–59.
- [40] Qingxiao Sun, Yi Liu, Hailong Yang, Zhonghui Jiang, Zhongzhi Luan, and Depei Qian. 2023. Adaptive auto-tuning framework for global exploration of stencil optimization on gpus. *IEEE Transactions on Parallel and Distributed Systems* 35, 1 (2023), 20–33.
- [41] Sven Verdoolaege, Juan Carlos Juega, Albert Cohen, Jose Ignacio Gomez, Christian Tenllado, and Francky Catthoor. 2013. Polyhedral parallel code generation for CUDA. *ACM Transactions on Architecture and Code Optimization (TACO)* 9, 4 (2013), 1–23.
- [42] Samuel Williams, Andrew Waterman, and David Patterson. 2009. Roofline: an insightful visual performance model for multicore architectures. *Commun. ACM* 52, 4 (April 2009), 65–76. doi:10.1145/1498765.1498785
- [43] Michael Wolfe. 1989. More iteration space tiling. In *Proceedings of the 1989 ACM/IEEE conference on Supercomputing*. 655–664.
- [44] Michael Joseph Wolfe. 1995. *High performance compilers for parallel computing*. Addison-Wesley Longman Publishing Co., Inc.
- [45] Xin You, Hailong Yang, Zhonghui Jiang, Zhongzhi Luan, and Depei Qian. 2021. DRStencil: Exploiting data reuse within low-order stencil on GPU. In *2021 IEEE 23rd Int Conf on High Performance Computing & Communications; 7th Int Conf on Data Science & Systems; 19th Int Conf on Smart City; 7th Int Conf on Dependability in Sensor, Cloud & Big Data Systems & Application (HPCC/DSS/SmartCity/DependSys)*. IEEE, 63–70.
- [46] Liang Yuan, Yunquan Zhang, Peng Guo, and Shan Huang. 2017. Tessellating stencils. In *Proceedings of the International Conference for High Performance Computing, Networking, Storage and Analysis*. 1–13.
- [47] Lingqi Zhang, Jiajun Huang, Sheng Di, Satoshi Matsuoka, and Mohamed Wahib. 2025. Can Tensor Cores Benefit Memory-Bound Kernels? (NO!). In *Proceedings of the 17th Workshop on General Purpose Processing Using GPU (GPGPU '25)*. Association for Computing Machinery, New York, NY, USA, 28–34. doi:10.1145/3725798.3725803
- [48] Lingqi Zhang, Mohamed Wahib, Peng Chen, Jintao Meng, Xiao Wang, Toshio Endo, and Satoshi Matsuoka. 2023. Revisiting temporal blocking stencil optimizations. In *Proceedings of the 37th International Conference on Supercomputing*. 251–263.
- [49] Yiwei Zhang, Kun Li, Liang Yuan, Jiawen Cheng, Yunquan Zhang, Ting Cao, and Mao Yang. 2024. LoRAStencil: Low-Rank Adaptation of Stencil Computation on Tensor Cores. In *SC24: International Conference for High Performance Computing, Networking, Storage and Analysis*. IEEE, 1–17.
- [50] Tuowen Zhao, Protonu Basu, Samuel Williams, Mary Hall, and Hans Johansen. 2019. Exploiting reuse and vectorization in blocked stencil computations on CPUs and GPUs. In *Proceedings of the International Conference for High Performance*

Computing, Networking, Storage and Analysis. 1–44.